Azimuthal Anisotropy of the Crust and Uppermost Mantle beneath Alaska

L. Feng[a *] and M.H. Ritzwoller[a]

[a] Department of Physics, University of Colorado at Boulder, Boulder, CO 80301

*Corresponding author: Lili Feng (lili.feng@colorado.edu).

Key Words: Seismic anisotropy, seismic surface wave tomography, crustal and mantle structure, crustal and mantle deformation, Alaska

Abstract

This study presents a shear wave azimuthally anisotropic model of the crust and uppermost mantle beneath Alaska and surroundings, based on Rayleigh wave phase speed measurements from 10 to 80 s period determined from recordings of ambient noise and earthquakes observed at more than 500 broadband stations. We test the hypothesis that a model composed of two homogeneous layers of anisotropy can explain these measurements. This "Simplified Two-Layer Model" confines azimuthal anisotropy to the brittle upper crust above 15 km along with the uppermost mantle from the Moho to 200 km. This model passes the hypothesis test for most of the region of study, from which we draw two conclusions. (a) The data are consistent with crustal azimuthal anisotropy being dominantly controlled by deformationally-aligned cracks and fractures in the upper crust undergoing brittle deformation. (b) They are also consistent with the uppermost mantle beneath Alaska and surroundings experiencing vertically coherent deformation. There are two exceptions to the latter conclusion (the Alexander and Koyukuk terranes) where two anisotropic layers in the mantle are required to fit the data. The model resolves several prominent features. (1) In the upper crust, fast directions are principally aligned with the orientation of major faults. (2) In the upper mantle, fast directions are aligned with the compressional direction in compressional domains and are parallel to the tensional direction in tensional domains. (3) The mantle fast directions located near the Alaska-Aleutian subduction zone and the surrounding back-arc area compose a toroidal pattern that is consistent with mantle flow directions predicted by geodynamical models. Finally, the mantle part of the model is remarkably consistent with SKS fast directions, but the fit to SKS splitting times would require anisotropy to extend below 200 km across most of the study region.

1 Introduction

Alaska occupies a region that includes a large subduction zone, the major rotational province of Arctic Alaska (e.g., Moore and Box, 2016), areas having undergone and continuing to undergo extensional tectonics (e.g., Johnston, 2001), and the successive accretion of terranes along both convergent and strike-slip fault zones (e.g., Coney & Jones, 1985; Johnston, 2001). The active Alaska-Aleutian subduction zone along the southern margin of Alaska is particularly complex with on-going subduction of the Pacific plate and collisional processes produced by the Yakutat microplate (e.g., Eberhart-Philips et al., 2006). At present, different parts of Alaska continue to move relative to the stable North America plate and significant seismicity is found across most of the state (e.g., Freymueller et al., 2008). The seismic data collected by the recently deployed EarthScope USArray Transportable Array (TA) and other local networks (**Figure 1**) provide the unprecedented opportunity to model and understand structures and dynamical processes beneath Alaska in much greater detail.

Previous seismic studies of the crust and mantle beneath Alaska have been based on a variety of types of data and techniques; however, most have focused on determining isotropic seismic structure (e.g., Jiang et al., 2018; Martin-Short et al., 2018; Ward & Lin, 2018). Studies of anisotropy have been based primarily on shear wave splitting (e.g., Yang & Fischer, 1995; Wiemer et al., 1999; Christensen & Abers, 2010; Hanna & Long, 2012; Venereau et al., 2019), although a few used surface waves (e.g., Wang & Tape, 2014; Feng & Ritzwoller, 2019) or body waves (e.g., Gou et al., 2019). Seismic anisotropy, in comparison with isotropic structure, is a second-order feature and its observation is challenging. However, it is important because it can provide information about past and present-day deformation in the crust and mantle (e.g., Crampin, 1984; Savage et al., 1990; Babuska and Cara, 1991; Vinnik et al., 1992; Savage, 1994; Silver, 1996; Long & Silver, 2008; Long, 2013).

Among recent surface wave studies of anisotropy beneath Alaska, Feng & Ritzwoller (2019) present a 3-D model that includes apparent radial anisotropy of shear wave speed (Vsv, Vsh) in the crust and uppermost mantle beneath Alaska. The inferred apparent crustal radial anisotropy is strongest across the parts of central and northern Alaska that were subject to large magnitude mid-Cretaceous extension. This is consistent with the crustal radial anisotropy being caused by deformationally-oriented middle to lower crustal sheet silicates (micas) with shallowly dipping foliation planes beneath extensional domains (e.g., Shapiro et al., 2004; Moschetti et al., 2010; Hacker et al., 2014).

This paper complements the study of Feng & Ritzwoller (2019) by presenting a model of azimuthal anisotropy in the crust uppermost mantle. The model is based on the azimuthal variation of ambient noise and earthquake derived Rayleigh wave phase speed measurements from 10 to 80 s observed at TA stations as well as other permanent and temporary networks in and around Alaska (**Fig. 1**). In particular, we test the hypothesis that the data can be fit with a "two-layer" model in which azimuthal anisotropy is confined to the upper crust to a depth of 15 km and a single depth-invariant layer in the mantle from the Moho to a depth of 200 km. Confining azimuthal anisotropy to the brittly-deforming upper crust is motivated by earlier studies in the US, Tibet, and Alaska (e.g., Shapiro et al., 2004; Moschetti et al., 2010; Lin et al., 2011; Xie et al., 2015, 2017; Feng & Ritzwoller, 2019). The single layer in the mantle is chosen for simplicity rather than preference. We refer to the model that results as the "Simplified Two-Layer model".

As discussed by Feng & Ritzwoller (2019), when inferring anisotropy using surface waves, it is useful to bear in mind two coordinate systems. The first is the frame defined by a symmetry axis (or foliation plane) of the medium of transport, in which "inherent" anisotropy is defined, and the second is the frame of the observations where "apparent" anisotropy is defined. We follow Xie et al. (2017) and refer to measurements of anisotropy and inferences drawn from them in the observational frame as "apparent". Apparent shear wave azimuthal anisotropy refers to dependence of propagation speed on azimuth. A common measure of the apparent shear wave azimuthal anisotropy is the fast azimuth φ_{SV} and amplitude A_{SV} of anisotropy, where the subscript "SV" means that anisotropy is in Vsv. The fast azimuth φ_{SV} defines the direction in which the Rayleigh wave propagates with fastest speed and the anisotropy amplitude A_{SV} depicts the strength of the anisotropy in the fast azimuth direction.

Most studies of anisotropy, including this paper and the study of Feng & Ritzwoller (2019), report measurements and models of particular aspects of apparent anisotropy. In contrast, Xie et al. (2015, 2017) present methods that use observations of apparent radial and azimuthal anisotropy to infer characteristics of the depth-dependent elastic tensor, which possesses information about inherent anisotropy. The inference of inherent anisotropy is beyond the scope of this paper, however.

The paper is organized as follows. In section 2 we present information about the data sets and the tomographic method, including how we estimate uncertainties in the Rayleigh wave phase speed measurements and the quantities inferred from them (e.g., A_{SV}, φ_{SV}). Section 3 presents examples of the 2-D Rayleigh wave azimuthally anisotropic phase speed maps along with corresponding uncertainties, and section 4 shows how the azimuthally anisotropic model is produced by using the first-order perturbation theoretic method of Montagner & Nataf (1986) to fit the azimuthal variation of dispersion data and uncertainties extracted from the tomographic maps. We present the features revealed by the model in section 5 and discuss them in section 6.

2 Data Set and Tomographic Method

This study uses the Rayleigh wave phase speed dispersion measurements (10 to 80 s) produced by Feng & Ritzwoller (2019), which derive from both ambient noise cross-correlation and earthquake waveforms. The seismic records are extracted from 22 permanent and temporary networks deployed across Alaska and northwest Canada between January 2001 and February 2019 (**Fig. 1**), totaling 537 seismic stations in total. More detailed information about the seismic arrays and data processing procedures is presented by Feng & Ritzwoller (2019).

Based on measurements of Rayleigh wave phase time, we perform eikonal tomography (Lin et al., 2009), a geometrical ray theoretic method, to estimate local azimuthally-dependent Rayleigh wave phase speed and associated uncertainty from ambient noise and earthquake dispersion data on a spatial grid of about 20 km. To estimate the azimuthal variation of phase speed, we stack all phase speed versus azimuth measurements on a coarser spatial grid with a spacing of about 200 km and average the measurements in 18 degree azimuthal bins. This improves spatial coverage and reduces the scatter in the measurements, but at the expense of degrading the spatial resolution. **Figure 2** presents examples of the resulting azimuthal variation of phase speed for two sample grid points, A and B identified in **Figure 1**. For weakly anisotropic media, the azimuthally binned Rayleigh wave phase speed measurements can be fit with a sinusoidal function (Smith and Dahlen, 1973), which indicates the so-called 2-ψ azimuthal variation:

$$C(\omega, \psi) = C_{iso}(\omega)\{1 + A(\omega)\cos[2(\psi - \varphi_{FA}(\omega))]\} \quad (1)$$

where ψ is the azimuth, ω is the angular frequency, C_{iso} is the isotropic phase speed, $\varphi_{FA}(\omega)$ is the fast azimuth of "2-ψ" anisotropy, and $A(\omega)$ is the amplitude of 2-ψ anisotropy. Estimates of

$\varphi_{FA}(\omega)$ and $A(\omega)$ with corresponding uncertainties, computed by standard normal error propagation from the measured to inferred quantities, are annotated on the panels of **Figure 2**.

Lin & Ritzwoller (2011) reported that a 1-ψ pattern in the phase speed measurements can be observed for long period surface waves near strong isotropic structural gradients caused by backscattering in heterogeneous isotropic media. This effect may contaminate estimates of $\varphi_{FA}(\omega)$ and $A(\omega)$, particularly at long periods (>50 s). Because we also observe strong 1-ψ patterns at long periods in some places, we simultaneously estimate the 1-ψ and 2-ψ components, as suggested by Lin & Ritzwoller (2011), but report only the 2-ψ component.

The reliability of the estimates of 2-ψ azimuthal anisotropy can be assessed by comparing estimates of $\varphi_{FA}(\omega)$ and $A(\omega)$ determined separately from ambient noise and earthquake datasets. In **Figure 3**, we compare the azimuthal anisotropy maps at 30 s period from ambient noise tomography (ANT) and earthquake tomography (ET). The fast azimuths yielded by ANT and ET are largely consistent (**Fig. 3a** and **Fig. 3b**). Indeed, **Figure 3c** shows the angle differences in fast azimuth, and the corresponding histogram (**Fig. 3d**) indicates that at more than 80 % of the locations there is an angle difference smaller than 30°. Large differences in fast azimuth are located in the northern and southern parts of the study region, where the strength of anisotropy is weaker and azimuthal coverage is less complete. A comparison with similar results was performed for the western United States by Lin et al. (2011).

Final maps of fast axis, $\varphi_{FA}(\omega)$, and anisotropy amplitude, $A(\omega)$, combine the measurements from ambient noise and earthquakes rather than performing tomography for each data set separately. At periods from 10 – 18 s, there are only ambient noise measurements, but from 20 – 60 s the measurements are combined from ambient noise and earthquakes. For periods above 60 s, there are only earthquake measurements. The combination of the two types of measurements (ambient noise and earthquake travel times) significantly improves the azimuthal coverage of the phase speed measurements and thus enhances the quality of the estimates of azimuthal anisotropy. Examples of the final data set are presented with azimuth- and amplitude-dependent bars at periods of 10, 30, 60, and 80 s in **Figure 4**.

We estimate azimuthally-dependent uncertainties in the phase speed measurements (e.g., **Fig. 2**) by taking the standard deviation of the mean in each azimuthal bin at each location and period. Uncertainties in $\varphi_{FA}(\omega)$ and $A(\omega)$ are derived values, estimated by error propagation in the regression for these quantities. Lin et al. (2009) argue that the uncertainties in isotropic phase speeds are underestimated by this procedure, which does not account for systematic errors or the correlation of errors for different measurements at different periods. We agree that uncertainties in $\varphi_{FA}(\omega)$ and $A(\omega)$ are probably underestimated, and we scale up uncertainties in each quantity so that about two-thirds of the uncertainty values are larger than the differences between ambient noise and earthquake based estimates of $\varphi_{FA}(\omega)$ and $A(\omega)$ across the region of study. We scale up the uncertainty in fast azimuth, $\varphi_{FA}(\omega)$, by a factor of 3.5 and in amplitude, $A(\omega)$ by a factor of 4.0. The up-scaled values are reflected in the uncertainty maps shown in **Figure 5** and other figures.

3 Rayleigh Wave Azimuthal Anisotropy

From 10-30 s period, where Rayleigh waves are primarily sensitive to crustal structure, the patterns of the fast directions of azimuthal anisotropy are similar to one another in the interior of Alaska. **Figures 4a** and **4b** present examples at 10 and 30 s period. Fast direction run nearly parallel to the principal local orientation of major faults, which may result from the generation of crustal azimuthal anisotropy from deformationally-oriented cracks and fractures. In contrast, at longer periods (e.g., 60 s in **Fig. 4c**) which are more sensitive to the mantle, there is a large-scale rotational pattern in the fast axis distribution, apparently caused by the subducting Pacific slab. Together with the high-speed slab anomaly, this rotational pattern moves northward at 80 second period (**Fig. 4d**). Patterns of fast directions similar to this have been reported by previous studies of SKS splitting (e.g., Christensen & Abers, 2010; Hanna & Long, 2012; Perttu et al., 2014; Venereau et al., 2019).

Examples of estimates of uncertainties (appropriately upscaled) in fast azimuth and the amplitude of anisotropy are presented in **Figure 5**. Uncertainties are smallest at 30 s period because high quality data from both ambient noise and earthquakes exist at this period, similar to uncertainties of isotropic shear wave speeds (Feng & Ritzwoller, 2019). Uncertainties in fast azimuth estimates maximize locally where anisotropy amplitudes are smallest.

From the Rayleigh wave azimuthal anisotropy maps, we extract local azimuthal anisotropy dispersion curves on a 200-km grid across the study region. These curves are the basis for the inversion for shear wave azimuthal anisotropy in the crust and mantle. Example azimuthal anisotropy dispersion curves along with corresponding uncertainties for the sample points A – D, identified in **Figure 1**, are shown in **Figure 6**. The period-dependence of these curves provides the depth resolution in this study, where crustal anisotropy is dominantly constrained by measurements below about 30 s and mantle anisotropy is determined by the longer period measurements.

4 Inversion Procedure

4.1 Model parameterization

As discussed in the Introduction, the inversion tests the hypothesis that azimuthal anisotropy is principally confined to two vertically homogeneous layers: the upper crust from the base of the sediments to a depth of 15 km and the mantle from the Moho to 200 km depth. Under this hypothesis, crustal anisotropy at depths less than 15 km is produced primarily by brittle deformation, which generates oriented cracks and fractures at multiple length-scales (e.g., Crampin, 1984). Mantle azimuthal anisotropy may also be strong, being caused by the lattice-preferred orientation (LPO) of olivine, associated with large-scale deformation and mantle flow. We do not include azimuthal anisotropy in the sediments or in the lower crust, where we hypothesize that azimuthal anisotropy is relatively weak across the region of study and anisotropy is largely radial at these depths. Thus, we parametrize the Simplified Two-Layer Model with two independent anisotropic layers with depth-independent anisotropy in each**.** The inferred model comprises two pairs of anisotropy values at each location, fast azimuth φ_{SV} and anisotropy amplitude A_{SV}: namely, $(\varphi_{SV}^{(1)}, A_{SV}^{(1)})$ in the upper crust and $(\varphi_{SV}^{(2)}, A_{SV}^{(2)})$ in the mantle. The symbols φ_{SV} and A_{SV} are depth-dependent quantities that are distinct from the symbols for frequency-dependent fast azimuth and anisotropy amplitude of Rayleigh waves, namely $\varphi_{FA}(\omega)$ and $A(\omega)$.

4.2 Inversion scheme

The inversion scheme is similar to that used in the studies of Yao et al. (2010) and Lin et al. (2011). It is based on the first-order perturbation theory presented by Montagner & Nataf (1986), which describes the azimuthal variation of Rayleigh wave phase speed, C_R, as:

$$\delta C_R(\omega, \psi) = \int_0^H \{(B_c \cos 2\psi + B_s \sin 2\psi)\frac{\partial C_R}{\partial A}|_0 + (G_c \cos 2\psi + G_s \sin 2\psi)\frac{\partial C_R}{\partial L}|_0$$

$$+(H_c \cos 2\psi + H_s \sin 2\psi)\frac{\partial C_R}{\partial F}|_0\}dz \qquad (2)$$

In eq. (2), B_c, B_s, G_c, G_s, H_c and H_s are linear combinations of the components of the azimuthally variable parts of the elastic modulus matrix and $\frac{\partial C_R}{\partial A}|_0$, $\frac{\partial C_R}{\partial L}|_0$ and $\frac{\partial C_R}{\partial F}|_0$ are the sensitivity kernels for three of the five elastic parameters ($A = \rho V_{PH}^2, C = \rho V_{PV}^2, N = \rho V_{SH}^2, L = \rho V_{PV}^2$, and F) that describe transversely isotropic (TI) media.

In the end, we omit the $\mathrm{H_c}$ and $\mathrm{H_s}$ terms, which provide sensitivity to the elastic modulus F, because their impact on Rayleigh wave phase speed is considered smaller based on empirical mineralogical models (Montagner & Nataf, 1986). Similar to Lin et al. (2011) and based on studies of olivine (Montagner & Nataf, 1986) as well as mica and amphibole in crustal rocks (Barruol & Kern, 1996), we assume that $\mathrm{B_{c,s}/A = G_{c,s}/L}$. Thus, eq. (2) can be simplified as:

$$\delta \mathrm{C_R}(\omega, \psi) = \int_0^{\mathrm{H}} \{\mathrm{G_c} \cos 2\psi \left(\frac{\mathrm{A}}{\mathrm{L}} \frac{\partial \mathrm{C_R}}{\partial \mathrm{A}} |_0 + \frac{\partial \mathrm{C_R}}{\partial \mathrm{L}} |_0 \right) + \mathrm{G_s} \sin 2\psi \left(\frac{\mathrm{A}}{\mathrm{L}} \frac{\partial \mathrm{C_R}}{\partial \mathrm{A}} |_0 + \frac{\partial \mathrm{C_R}}{\partial \mathrm{L}} |_0 \right) \} dz \tag{3}$$

Given the reference velocity model constructed by Feng & Ritzwoller (2019), we use a transversely isotropic forward code (Herrmann, 2013) with earth flattening to compute numerically the depth-dependent sensitivity kernels for the moduli A and L (e.g., Xie et al., 2015). The resulting sensitivity kernel, which we will refer to as $K(z)$ for the effective moduli $\mathrm{G_c}$ (or $\mathrm{G_s}$), is K(z) = (A/L)$\partial \mathrm{C_R}/\partial A + \partial \mathrm{C_R}/\partial L$. Because the modulus A is related to $\mathrm{V_{PH}}$ and L is related to $\mathrm{V_{SV}}$, K(z) is sensitive both to anisotropy in both compressional and shear wave speeds. Amplitude normalized examples of $K(z)$ at four periods are presented in **Figure 7**. The shallower part of the kernel is more sensitive to $\mathrm{V_{PH}}$ and the deeper parts are more sensitive to $\mathrm{V_{SV}}$. Thus, the data we use are more sensitive to azimuthal anisotropy in $\mathrm{V_{PH}}$ in the crust and $\mathrm{V_{SV}}$ in the mantle.

We use the observed azimuthal anisotropy dispersion curves of $\varphi_{\mathrm{FA}}(\omega)$ and $\mathrm{A}(\omega)$ (e.g., **Fig. 6**) to estimate $(\mathrm{G_c^{(1)}}, \mathrm{G_s^{(1)}})$ and $(\mathrm{G_c^{(2)}}, \mathrm{G_s^{(2)}})$ in the upper crust and mantle simultaneously by linear inversion. Similar to Yao et al. (2010), the fast azimuth φ_{SV} and anisotropy amplitude $\mathrm{A_{SV}}$ are determined from the moduli $\mathrm{G_c}$ and $\mathrm{G_s}$as follows for the upper crust and mantle:

$$\varphi_{SV} = \frac{1}{2}\tan^{-1}(\frac{G_s}{G_c}) \tag{4}$$

and

$$A_{SV} = \frac{1}{2L}\sqrt{G_c^2 + G_s^2} \tag{5}$$

Corresponding uncertainties are determined from the estimated model covariance matrix (Tarantola, 2005).

5 Results

The resulting two-layer model, namely, $(\varphi_{SV}^{(1)}, A_{SV}^{(1)})$ in the upper crust to 15 km and $(\varphi_{SV}^{(2)}, A_{SV}^{(2)})$ in the mantle to 200 km, is shown in **Figure 8**. Consistent with the shorter period Rayleigh wave observations, the upper crustal fast directions are principally aligned with the major faults, as discussed further in section 6.1. In contrast, the distribution of mantle fast directions is similar to the longer period observations and results in a different pattern that is discussed further in section 6.2.

The average amplitude of anisotropy is stronger in the crust than in the mantle, averaging 1.3% in the crust and 0.4% in the mantle. Correspondingly, the length references for the bars differ between **Figure 8a** and **8b**, being 3% **in Figure 8a** and 1s% in **Figure 8b**. Uncertainty in the fast directions maximizes where the amplitudes of anisotropy minimize and also tends to be larger near the periphery of the region of study where azimuthal coverage degrades. For this reason, the patterns of fast axis uncertainty are not particularly informative, but we note that the one standard deviation uncertainty for fast axis averages about 8^{o} in the crust across the region of study and about 13^{o} in the mantle. The one standard deviation uncertainty for the amplitude of azimuthal anisotropy averages about half of the average value across the region of study: 0.7% for the crust and 0.2% for the mantle.

We are interested in testing the null hypothesis that the Simplified Two-Layer Model can fit the data acceptably, and as well as other and more complicated distributions of anisotropy in the crust and mantle. Misfits of observations of fast azimuth and anisotropy amplitude by predictions from the resulting two-layer model are shown in **Figure 9**. We define the misfit as follows:

$$\chi = \sqrt{\frac{1}{N}\sum_{i=1}^{N}\frac{(\Delta d_i)^2}{\sigma_i^2}} \tag{6}$$

where Δd_i is the difference between an observed datum (fast azimuth or anisotropy amplitude) and the value predicted by the model, and σ_i is the one standard deviation data uncertainty. The index i ranges over dispersion values from that location, namely $\varphi_{FA}(\omega)$ and $A(\omega)$, where N is the number of the data values. Δd_i for fast azimuth is defined as:

$$\Delta d_i = \begin{cases} \left|\varphi_i^{obs} - \varphi_i^{pre}\right|, & if \left|\varphi_i^{obs} - \varphi_i^{pre}\right| \leq 90° \\ 180° - \left|\varphi_i^{obs} - \varphi_i^{pre}\right|, & if \left|\varphi_i^{obs} - \varphi_i^{pre}\right| > 90° \end{cases} \tag{7}$$

where φ_i^{obs} is the observed fast azimuth and φ_i^{pre} represents the predicted value. For anisotropy amplitude, Δd_i is defined as follows:

$$\Delta d_i = A_i^{obs} - A_i^{pre} \tag{8}$$

where A_i^{obs} is the observed anisotropy amplitude and A_i^{pre} indicates the predicted value.

The Simplified Two-Layer Model can fit the amplitude of Rayleigh wave anisotropy across essentially the entire region of study (**Fig. 9b**) and predict the Rayleigh wave fast azimuth directions across most of the region of study (**Fig. 9a**). Thus, for the amplitude of azimuthal anisotropy, the null-hypothesis is confirmed; no model of anisotropy more complicated than the Simplified Two-Layer Model is needed to fit observations of the amplitude of azimuthal anisotropy. Misfit in fast azimuth (**Fig. 9a**) is substantial only in the Alexander and Koyukuk terranes (identified as points C and D in **Fig. 1**). In fact, as shown in **Figures 9c-d**, fast azimuth misfit is confined principally to periods above 40 s, consistent with the need to add a second mantle layer in these two terranes. Therefore, the null-hypothesis is confirmed for the fast azimuth of anisotropy across most of Alaska, but is overturned in the Alexander and Koyukuk terranes where an additional mantle layer is required to fit the data, as discussed further in section 6.2.5.

6 Discussion

6.1 Crustal Anisotropy

The Simplified Two-Layer Model fits the short period Rayleigh wave anisotropy information well in both fast axis direction (**Fig. 9c**) and amplitude (**Fig. 9b**). But are we justified to conclude from data fit alone that this is the correct depth distribution of azimuthal anisotropy? In a word – no. To demonstrate why, we consider candidate models in which the depth distribution of crustal azimuthal anisotropy differs from the Simplified Model, referred to as Alternative Models (AM) 1 - 3. These are: (AM1) only lower crustal anisotropy from a depth of 15 km to the Moho with no anisotropy in the upper crust, (AM2) the whole crust is a single uniform layer of anisotropy from the bottom of sediments to the Moho, and (AM3) there are two independent layers of crustal anisotropy where the upper crust to 15 km and the lower crust from 15 km to Moho are allowed to have different values of φ_{SV} and A_{SV}.

We find that the misfit provided by AM1 and AM2 (maps not shown) are nearly identical to that delivered by the Simplified Two-Layer Model. In addition, although AM4 adds degrees of freedom to improve data fit, there is very little improvement in the data fit (map not shown) compared to the Simplified Two-Layer Model. Improving the fit to fast axes requires additional layer(s) in the mantle not the crust, as discussed below. The similarity in misfit among these parameterizations of crustal anisotropy illustrates the intrinsic lack of depth resolution for crustal anisotropy provided by our dataset.

We find, therefore, that the Simplified Two-Layer Model is consistent with the data, but that upper crustal anisotropy is not necessary to fit the data. Our preference for crustal azimuthal anisotropy confined to the upper crust comes primarily from the similarity between the fast axis directions with the major fault orientations across the region of study as well as from studies elsewhere in the world (e.g., Shapiro et al., 2004; Moschetti et al., 2010; Lin et al., 2011; Xie et al., 2015, 2017; Feng & Ritzwoller, 2019). In this view, crustal azimuthal anisotropy is produced principally by deformationally-aligned cracks and fractures in the upper crust undergoing brittle deformation.

In the future, it may be advantageous to apply methods like those of Xie et al. (2015, 2017) to estimate the depth-dependent elastic tensor by interpreting Rayleigh wave azimuthal anisotropy simultaneously with Love wave data (radial anisotropy), which may improve constraints on the depth distribution of crustal anisotropy.

6.2 Mantle Anisotropy

6.2.1 Data fit

A physically motivated layerization of uppermost mantle anisotropy might include two distinct depth zones, a lithosphere, which might represent frozen-in anisotropy, and an asthenosphere for anisotropy that evolves with the plate (e.g., Silver & Chan, 1988; Silver & Savage, 1994; Silver 1996). Instead, we first test whether a single mantle layer in which azimuthal anisotropy is constant from the Moho to a depth of 200 km in both fast-azimuth and amplitude will allow the data to be fit. **Figure 9d** shows that the one azimuthally anisotropic layer in the mantle in the Simplified Two-Layer Model can reasonably predict long period Rayleigh wave fast axis observations for most of the study region. Although more layers of anisotropy could be added and the data would still be fit, when they are introduced the model tends to oscillate vertically with successive layers having fast-axis directions that are nearly perpendicular to one another. The exception lies in the Alexander and Koyukuk terranes (identified as C and D in **Fig. 1**) where two layers of anisotropy are needed to fit the long period fast axis directions.

6.2.2 Patterns of fast directions in the mantle

Patterns of mantle fast directions vary regionally and change in a way that is correlated with changes in isotropic shear wave speeds. The large-scale high velocity isotropic anomalies occur in the compressional regions of the mantle, which include Arctic Alaska and the Pacific subduction zone, and in the North American Craton. Fast directions are generally oriented approximately along the compressional direction in each of these regions, nearly parallel to the gradient in shear wave speed. In particular, the fast directions in the slab region and back-arc area are related to the slab geometry, being approximately slab-perpendicular in the subduction zone and then shift to a slab-surrounding pattern in the back-arc region. Together, this transition in fast directions composes a toroidal pattern around the slab edge. This is consistent with the toroidal mantle flow directions around Alaskan slab edge predicted by geodynamical modeling (Jadamec & Billen, 2010).

In contrast, broadly speaking, the low speed region in the interior of Alaska undergoes tensional deformation (e.g., Redfield et al., 2007) and the fast directions are principally aligned with the directions of tensional deformation. Fast directions are more nearly perpendicular to the gradient in shear wave speed.

6.2.3 Vertical coherence of deformation?

If azimuthal anisotropy were vertically homogeneous in the mantle, then deformation may be vertically coherent. Our results are consistent with vertically homogeneous anisotropy from the Moho to 200 km across most of the study region with the two exceptions. This is not direct evidence for vertically coherent deformation because the data can be fit with anisotropy that differs between the lithosphere and the asthenosphere. However, we find no evidence against vertically coherent deformation in the mantle except in the Alexander and Koyukuk terranes. By "vertically coherent deformation" we mean in the mantle, as distinguished with the use of this term by Silver (1996), which refers to vertically coherent deformation in the crust and subcontinental mantle.

6.2.4 Comparison with SKS splitting

The mantle fast directions of the Simplified Two-Layer Model are consistent, on average, with SKS splitting results (Venereau et al., 2019), as shown in **Figure 10**. We discard data points from this comparison where the model uncertainty in fast azimuth is greater than 30° and where the amplitude of mantle anisotropy in our model is less than 0.3%. The yellow bars in **Figure 10a** show the orientation of fast directions of the mantle anisotropy in our model and the blue, green and red bars are the orientations of SKS splitting fast axes. Blue bars are locations where the differences between our model and SKS splitting observations are less than 30°, green bars where differences lie between 30° and 60°, and red bars where differences are greater than 60°. **Figure 10b** shows that approximately 88% of the SKS observations differ from our mantle fast directions by less than 30°.

The depths to which this similarity extends between our mantle model and SKS fast directions may be constrained by comparing the observed SKS splitting time with the prediction from our model. **Figure 10c** presents a histogram of the predicted SKS splitting time from the mantle part of our model from which the observed time is subtracted. The average SKS splitting time is 1.14 s. The observed SKS splitting times are larger than the values predicted from our model by an average of 0.66 s. Thus, the predicted splitting time averages about half of the observed SKS time (Venereau et al., 2019). It is likely, therefore, that there is a contribution to SKS splitting times deeper in the mantle (> 200 km) than our model extends, and that the fast-directions we observe in the mantle extend deeper than 200 km. Thus, any vertical coherence of deformation may extend past 200 km across most of Alaska.

6.2.5 Regions that require vertical inhomogeneity of mantle anisotropy and deformation

For the Alexander and Koyukuk terranes, significant improvement in data fit is achieved by adding an independent anisotropic layer below a depth of 100 km, but the fast azimuth of the upper layer is nearly perpendicular to that of the lower layer. We interpret these layers as being decoupled, and there is evidence in these regions that deformation is vertically inhomogeneous in the uppermost mantle. An example of the nature of this improvement in data fit is presented in **Figure 9c-d**.

In the Alexander Terrane, the fast directions in the lower layer in the mantle are similar to the SKS splitting results. We suggest that the SKS splitting in Alexander Terrane is dominantly controlled by the lower layer, which we interpret as the asthenosphere, and deformation in the lithosphere and asthenosphere are sub-perpendicular to each other. In the Koyukuk Terrane, the inversion yields a fast azimuth of 87° in the upper layer and 10° in the lower one. The lower layer's fast direction is similar to the fast direction in Arctic Alaska, to the north of this point. One possibility is that the layering is caused by underthrusting of Arctic Alaska beneath the Koyukuk Terrane, but isotropic shear wave speeds in the model of Feng & Ritzwoller (2019) do not provide support for this interpretation.

7. Conclusions

We present a shear wave azimuthally anisotropic model of the crust and uppermost mantle beneath Alaska. The model is represented by a two-layer parameterization of anisotropy where azimuthal anisotropy is confined to the brittle upper crust to a depth of 15 km and to the uppermost mantle from the Moho to 200 km depth. This study is essentially a hypothesis test and confirms that such a model can reasonably fit the observed azimuthal variation of Rayleigh wave phase speed measurements across most of the region of study. We refer to the resulting model as the Simplified Two-Layer Model.

The Rayleigh wave dispersion data are taken directly from the study of Feng & Ritzwoller (2019), which derives from waveforms of all broad-band seismic stations across the study region openly available from January 2001 to February 2019, totaling more than 500 stations taken from 22 networks (Transportable Array, Alaska Networks, etc.). The Rayleigh wave azimuthal anisotropy maps are constructed with eikonal tomography based on both ambient noise and earthquake tomography, extending from 10 to 80 s period. These data and corresponding uncertainties are the basis for the inversion for the azimuthally anisotropic model as a perturbation to a reference Vsv model across the study region.

The azimuthally anisotropic model derives from an inversion algorithm that is based on the first-order perturbation theory of Montagner & Nataf (1984), which relates the azimuthal variation in Rayleigh wave phase speed measurements with the azimuthal anisotropy of shear waves in the earth. The reference Vsv model that is used to compute the sensitivity kernels is from Feng & Ritzwoller (2019).

The Simplified Two-Layer Model is able to fit the Rayleigh wave azimuthal anisotropy data across the vast majority of the region of study, except for the Alexander Terrane and Koyukuk Terrane where an additional layer in the mantle is required to fit the long period data. A summary of our major findings and the structural features revealed by the azimuthally anisotropic model is as follows.

(1) In the crust, confining azimuthal anisotropy to the brittle upper crust allows the short period Rayleigh wave data to be fit. The resulting fast directions of the apparent crustal azimuthal anisotropy closely follow the orientation of major faults. These facts are consistent with crustal azimuthal anisotropy being dominantly caused by deformationally-aligned cracks and fractures (e.g., Crampin, 1984) in the shallow crust.

(2) For most of the region of study, the long period Rayleigh wave data can be fit using a single azimuthally anisotropic layer in the uppermost mantle extending from the Moho to a depth of 200 km. This result is consistent with but does not require vertical coherent deformation in the uppermost mantle beneath Alaska and surroundings. In addition, the fast directions in the model are largely consistent with SKS splitting fast direction (Venereau et al., 2019). Because the SKS delay times predicted from our model are significantly smaller than the observed values, we suggest that the coherence of mantle deformation may extend to depths greater than 200 km across much of the region of study.

(3) The fast directions in the mantle located at the Alaska-Aleutian subduction zone compose a toroidal pattern that is consistent with mantle flow directions predicted by geodynamical modelling (Jadamec & Billen, 2010). Azimuthal anisotropy in the back-arc area may be controlled by toroidal mantle flow.

(4) An additional anisotropic mantle layer is required to fit the long period Rayleigh wave observations in the Alexander Terrane and Koyukuk Terrane. The fast directions of the lower mantle layer in the Alexander Terrane are consistent with SKS splitting, producing two azimuthally anisotropic mantle layers with fast directions sub-perpendicular to each other.

In addition to providing information about crustal and mantle deformation and associated patterns of mantle flow pattern in the Alaskan-Aleutian subduction zone, the model we present here may usefully serve as a starting point for further studies, such as estimating the full depth-dependent elastic tensor in the crust and mantle (e.g., Xie et al., 2015, 2017). In this context, we strive to provide reliable information about model uncertainties across the region of study, which will help guide the future use of the model.

Acknowledgments

This research was supported by NSF grant EAR-1928395 at the University of Colorado at Boulder. The facilities of IRIS Data Services, and specifically the IRIS Data Management Center, were used for access to waveforms, related metadata and/or derived products used in this study. IRIS Data Services are funded through the Seismological Facilities for the Advancement of Geoscience and EarthScope (SAGE) Proposal of the National Science Foundation under Cooperative Agreement EAR-1261681. This work utilized the RMACC Summit supercomputer, which is supported by the National Science Foundation (awards ACI-1532235 and ACI-1532236), the University of Colorado Boulder, and Colorado State University. The Summit supercomputer is a joint effort of the University of Colorado Boulder and Colorado State University.

References

Babuska, V. and Cara, M., 1991. *Seismic anisotropy in the Earth* (Vol. 10). Springer Science & Business Media.

Barruol, G. and Kern, H., 1996. Seismic anisotropy and shear-wave splitting in lower-crustal and upper-mantle rocks from the Ivrea Zone—experimental and calculated data. *Phys. Earth Planet. Int.*, *95*(3-4), pp.175-194.

Christensen, D.H. and Abers, G.A., 2010. Seismic anisotropy under central Alaska from SKS splitting observations. *Journal of Geophysical Research: Solid Earth*, *115*(B4).

Coney, P.J. and Jones, D.L., 1985. Accretion tectonics and crustal structure in Alaska. *Tectonophysics*, *119*(1-4), pp.265-283.

Crampin, S., 1984. Effective anisotropic elastic constants for wave propagation through cracked solids. *Geophys. J. Int.*, *76*(1), pp.135-145.

Eberhart- Phillips, D., Christensen, D.H., Brocher, T.M., Hansen, R., Ruppert, N.A., Haeussler, P.J. and Abers, G.A., 2006. Imaging the transition from Aleutian subduction to Yakutat collision in central Alaska, with local earthquakes and active source data. *Journal of Geophysical Research: Solid Earth*, *111*(B11).

Feng, L. and Ritzwoller, M.H., 2019. A 3- D shear velocity model of the crust and uppermost mantle beneath Alaska including apparent radial anisotropy. *J. Geophys. Res.: Solid Earth*.

Freymueller, J.T., Woodard, H., Cohen, S.C., Cross, R., Elliott, J., Larsen, C.F., Hreinsdottir, S., Zweck, C., Haeussler, P.J., Wesson, R.L. and Ekström, G., 2008. Active deformation processes in Alaska, based on 15 years of GPS measurements. *Active tectonics and seismic potential of Alaska*, *179*, pp.1-42.

Gou, T., Zhao, D., Huang, Z. and Wang, L., 2019. Aseismic deep slab and mantle flow beneath Alaska: Insight from anisotropic tomography. *Journal of Geophysical Research: Solid Earth*, *124*(2), pp.1700-1724.

Hacker, B.R., Ritzwoller, M.H. & Xie, J., 2014. Central Tibet has a partially melted, mica-bearing crust, *Tectonics*, 33, doi:10.1002/2014TC003534.

Hanna, J. and Long, M.D., 2012. SKS splitting beneath Alaska: Regional variability and implications for subduction processes at a slab edge. *Tectonophys.*, *530*, pp.272-285.

Herrmann, R. B. 2013. Computer programs in seismology: An evolving tool for instruction and research. *Seism. Res. Lett.,* 84,1081–1088. https://doi.org/10.1785/0220110096

Jadamec, M. A., & Billen, M. I. 2010. Reconciling surface plate motions with rapid three-dimensional mantle flow around a slab edge. *Nature*, 465(7296), 338–341. https://doi.org/10.1038/nature09053

Jiang, C., Schmandt, B., Ward, K.M., Lin, F.C. and Worthington, L.L., 2018. Upper Mantle Seismic Structure of Alaska From Rayleigh and S Wave Tomography. *Geophysical Research Letters*, *45*(19), pp.10-350.

Johnston, S.T., 2001. The Great Alaskan Terrane Wreck: reconciliation of paleomagnetic and geological data in the northern Cordillera. *Earth and Planetary Science Letters*, *193*(3-4), pp.259-272.

Lin, F.C., Ritzwoller, M.H. and Snieder, R., 2009. Eikonal tomography: surface wave tomography by phase front tracking across a regional broad-band seismic array. *Geophys. J. Int.*, *177*(3), pp.1091-1110.

Lin, F.C., Ritzwoller, M.H., Yang, Y., Moschetti, M.P. and Fouch, M.J., 2011. Complex and variable crustal and uppermost mantle seismic anisotropy in the western United States. *Nature Geosci.*, *4*(1), p.55.

Lin, F.C. and Ritzwoller, M.H., 2011. Apparent anisotropy in inhomogeneous isotropic media. *Geophys. J. Int.*, *186*(3), pp.1205-1219.

Long, M.D. and Silver, P.G., 2008. The subduction zone flow field from seismic anisotropy: A global view. *Science*, *319*(5861), pp.315-318.

Long, M.D., 2013. Constraints on subduction geodynamics from seismic anisotropy. *Revs. of Geophys.*, *51*(1), pp.76-112.

Martin- Short, R., Allen, R., Bastow, I.D., Porritt, R.W. and Miller, M.S., 2018. Seismic imaging of the Alaska subduction zone: Implications for slab geometry and volcanism. *Geochemistry, Geophysics, Geosystems*, *19*(11), pp.4541-4560.

Montagner, J.-P. & Nataf, H.-C., 1986. A simple method for inverting the azimuthal anisotropy of surface waves, *J. Geophys. Res.,* 91(B1), 511, doi:10.1029/JB091iB01p00511.

Moore, T.E. and Box, S.E., 2016. Age, distribution and style of deformation in Alaska north of 60 N: Implications for assembly of Alaska. *Tectonophysics*, *691*, pp.133-170.

Moschetti, M.P., Ritzwoller, M.H., Lin, F. and Yang, Y., 2010. Seismic evidence for widespread western-US deep-crustal deformation caused by extension. *Nature*, *464*(7290), p.885.

Perttu, A., Christensen, D., Abers, G. and Song, X., 2014. Insights into mantle structure and flow beneath Alaska based on a decade of observations of shear wave splitting. *J. Geophys. Res.: Solid Earth*, *119*(11), pp.8366-8377.

Redfield, T.F., Scholl, D.W., Fitzgerald, P.G. and Beck Jr, M.E., 2007. Escape tectonics and the extrusion of Alaska: Past, present, and future. *Geology*, *35*(11), pp.1039-1042.

Savage, M.K., Silver, P.G. and Meyer, R.P., 1990. Observations of teleseismic shear- wave splitting in the Basin and Range from portable and permanent stations. *Geophys. Res. Letts.*, *17*(1), pp.21-24.

Silver, P.G. and Savage, M.K., 1994. The interpretation of shear-wave splitting parameters in the presence of two anisotropic layers. *Geophys. J. Int.l*, *119*(3), pp.949-963.

Savage, M.K., 1999. Seismic anisotropy and mantle deformation: what have we learned from shear wave splitting?. *Revs. of Geophys.*, *37*(1), pp.65-106.

Shapiro, N.M., Ritzwoller, M.H., Molnar, P. and Levin, V., 2004. Thinning and flow of Tibetan crust constrained by seismic anisotropy. *Science*, *305*(5681), pp.233-236.

Silver, P.G. and Chan, W.W., 1988. Implications for continental structure and evolution from seismic anisotropy. *Nature*, *335*(6185), p.34.

Silver, P.G., 1996. Seismic anisotropy beneath the continents: Probing the depths of geology. *Annual Review of Earth and Planetary Sciences*, *24*(1), pp.385-432.

Tarantola, A., 2005. *Inverse problem theory and methods for model parameter estimation* (Vol. 89). siam.

Smith, M.L. and Dahlen, F.A., 1973. The azimuthal dependence of Love and Rayleigh wave propagation in a slightly anisotropic medium. *J. Geophys. Res.*, *78*(17), pp.3321-3333.

Venereau, C.M.A., Martin- Short, R., Bastow, I.D., Allen, R.M. and Kounoudis, R., 2019. The Role of Variable Slab Dip in Driving Mantle Flow at the Eastern Edge of the Alaskan Subduction Margin: Insights From Shear- Wave Splitting. *Geochem., Geophys., Geosys.*

Vinnik, L.P., Makeyeva, L.I., Milev, A. and Usenko, A.Y., 1992. Global patterns of azimuthal anisotropy and deformations in the continental mantle. *Geophys. J. Int.*, *111*(3), pp.433-447.

Wang, Y. and Tape, C., 2014. Seismic velocity structure and anisotropy of the Alaska subduction zone based on surface wave tomography. *Journal of Geophysical Research: Solid Earth*, *119*(12), pp.8845-8865.

Ward, K.M. and Lin, F.C., 2018. Lithospheric structure across the Alaskan cordillera from the joint inversion of surface waves and receiver functions. *Journal of Geophysical Research: Solid Earth*, *123*(10), pp.8780-8797.

Wiemer, S., Tytgat, G., Wyss, M. and Duenkel, U., 1999. Evidence for shear-wave anisotropy in the mantle wedge beneath south central Alaska. *Bulletin of the Seismological Society of America*, *89*(5), pp.1313-1322.

Xie, J., Ritzwoller, M.H., Brownlee, S.J. and Hacker, B.R., 2015. Inferring the oriented elastic tensor from surface wave observations: preliminary application across the western United States. *Geophysical Journal International*, *201*(2), pp.996-1021.

Xie, J., M.H. Ritzwoller, W. Shen, and W. Wang, 2017. Crustal anisotropy across Eastern Tibet and surroundings modeled as a depth-dependent tilted hexagonally symmetric medium, *Geophys. J. Int.,* 209, 466-491, doi: 10.1093/gji/ggx004.

Yang, X., Fischer, K.M. and Abers, G.A., 1995. Seismic anisotropy beneath the Shumagin Islands segment of the Aleutian- Alaska subduction zone. *Journal of Geophysical Research: Solid Earth*, *100*(B9), pp.18165-18177.

Yao, H., Van Der Hilst, R.D. and Montagner, J.P., 2010. Heterogeneity and anisotropy of the lithosphere of SE Tibet from surface wave array tomography. *Journal of Geophysical Research: Solid Earth*, *115*(B12).

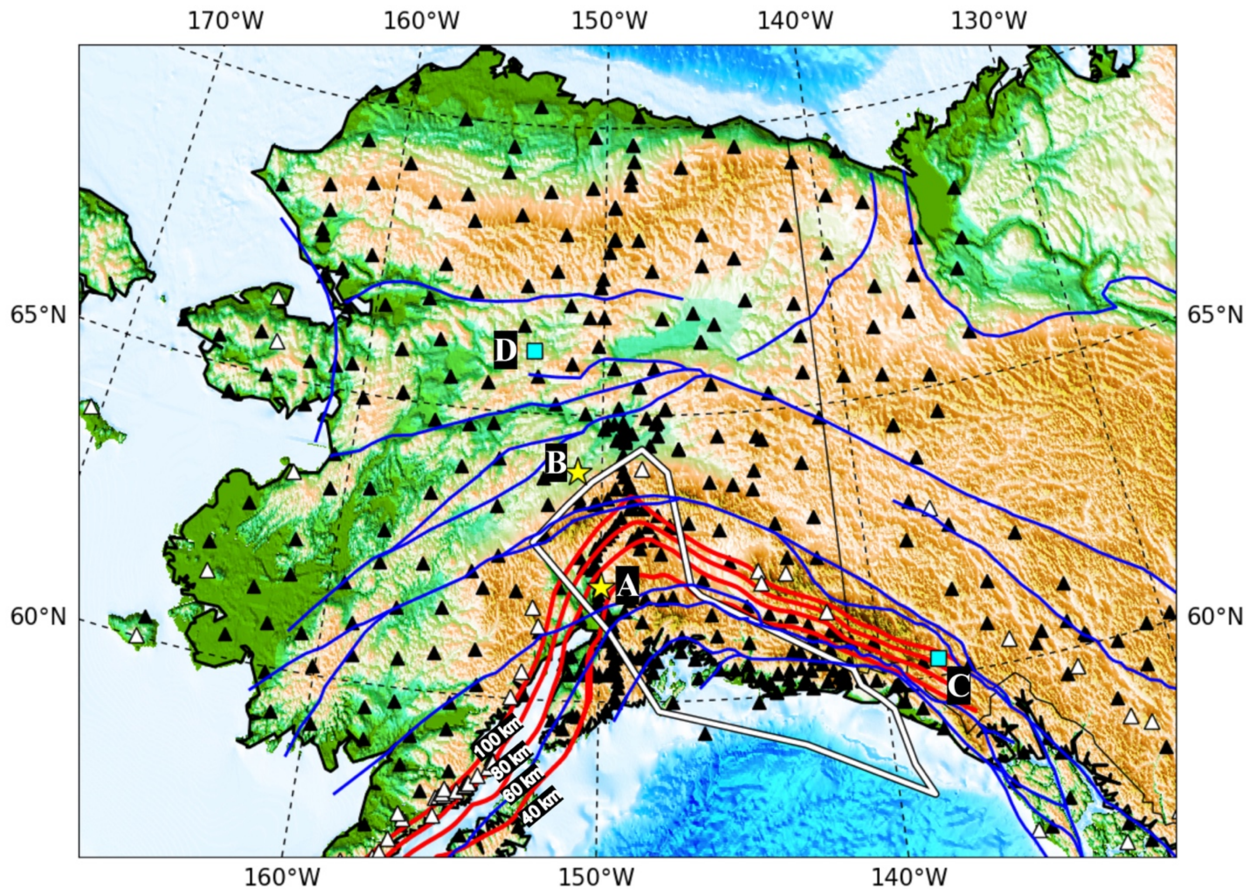

Figure 1. Seismic station distribution (black triangles) and volcanoes (white triangles) along with blue lines: major faults, red lines: the top of the subducting Alaskan-Aleutian slab at depths of 40, 60, 80, and 100 km (Jadamec and Billen, 2010), white polygon: the location of the hypothesized Yakutat Terrane (Eberhart-Phillips et al., 2006). Yellow stars are grid points located (A) south of Denali, north of the Cook Inlet and (b) north of Denali in the Yukon-Tanana terrane, referenced in **Figures 2 and 6a,b**. The cyan squares are locations used in **Figure 6c,d**, located in the (C) Alexander and (D) Koyukuk terranes where two mantle layers on anisotropy are needed to fit the data. Stations are identified with black triangles and volcanoes with white triangles.

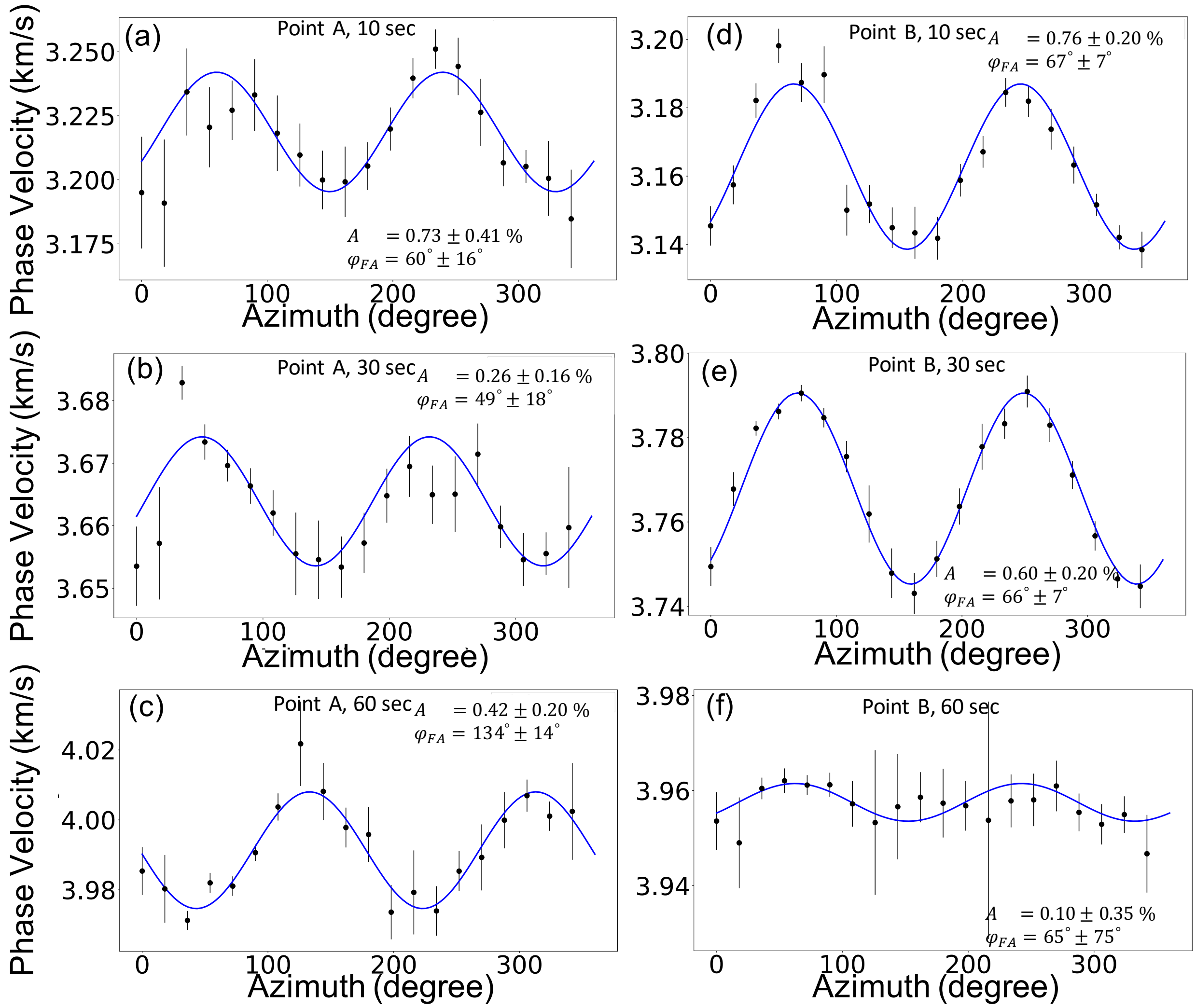

Figure 2. Azimuthal bin-averaged phase velocity measurements and bin standard deviations of the mean at periods of 10, 30, and 60 s plotted versus azimuth (**ψ**) measured using the eikonal tomography method at locations A and B identified in **Figure 1**. (a) – (c): Point A; (d) – (f): Point B. Fit amplitude and fast azimuth with one standard deviation uncertainties are indicated on each panel.

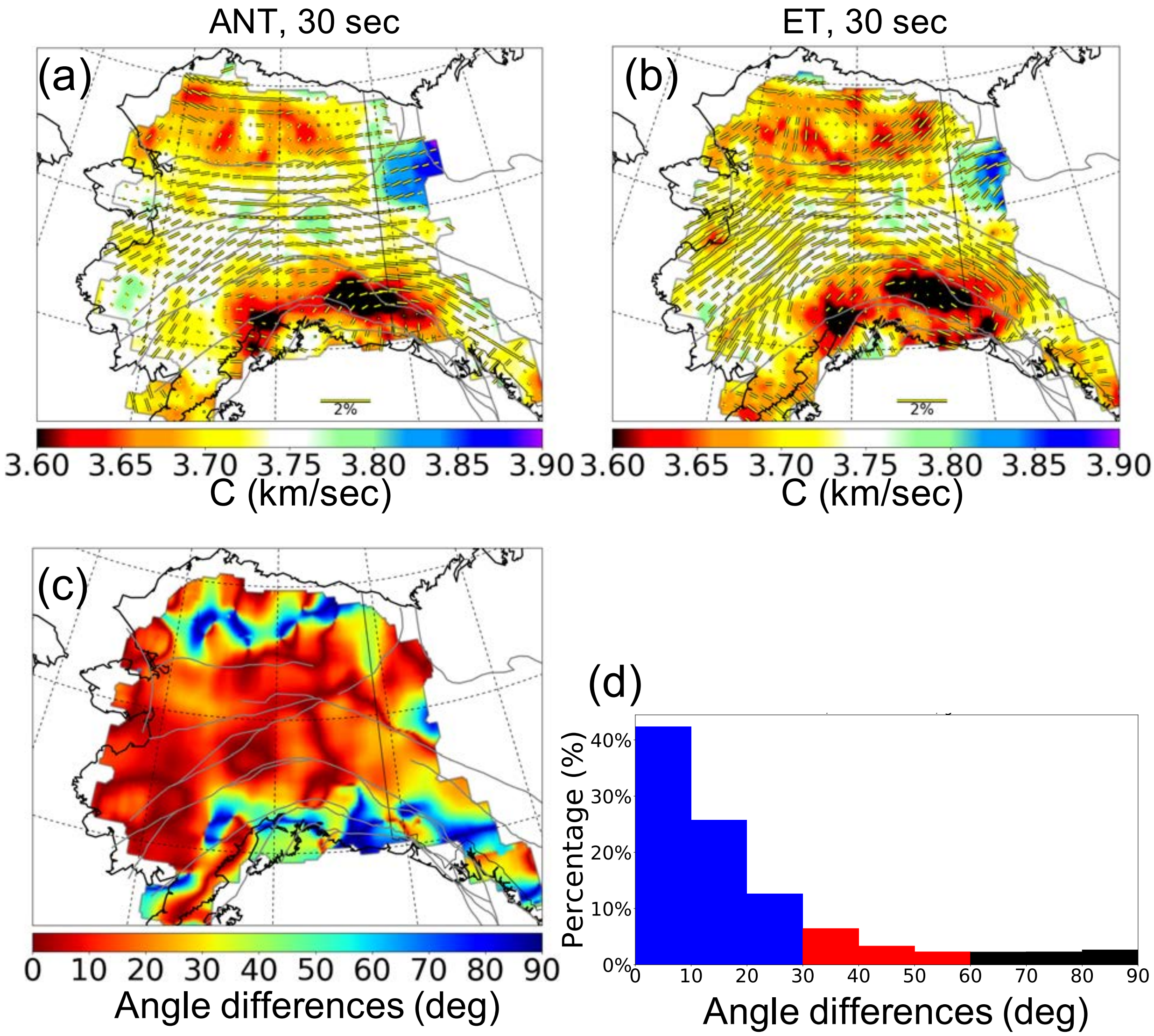

Figure 3. (a) Rayleigh wave phase speed at a period of 30 s along with the amplitude and fast axis directions for azimuthal anisotropy constructed with ambient noise tomography (ANT). (b) Similar to (a), but constructed by earthquake tomography (ET). (c) The fast axis angle differences between ANT and ET. (d) Corresponding histogram of (c). More than 80 % of locations have an angular difference less than 30°.

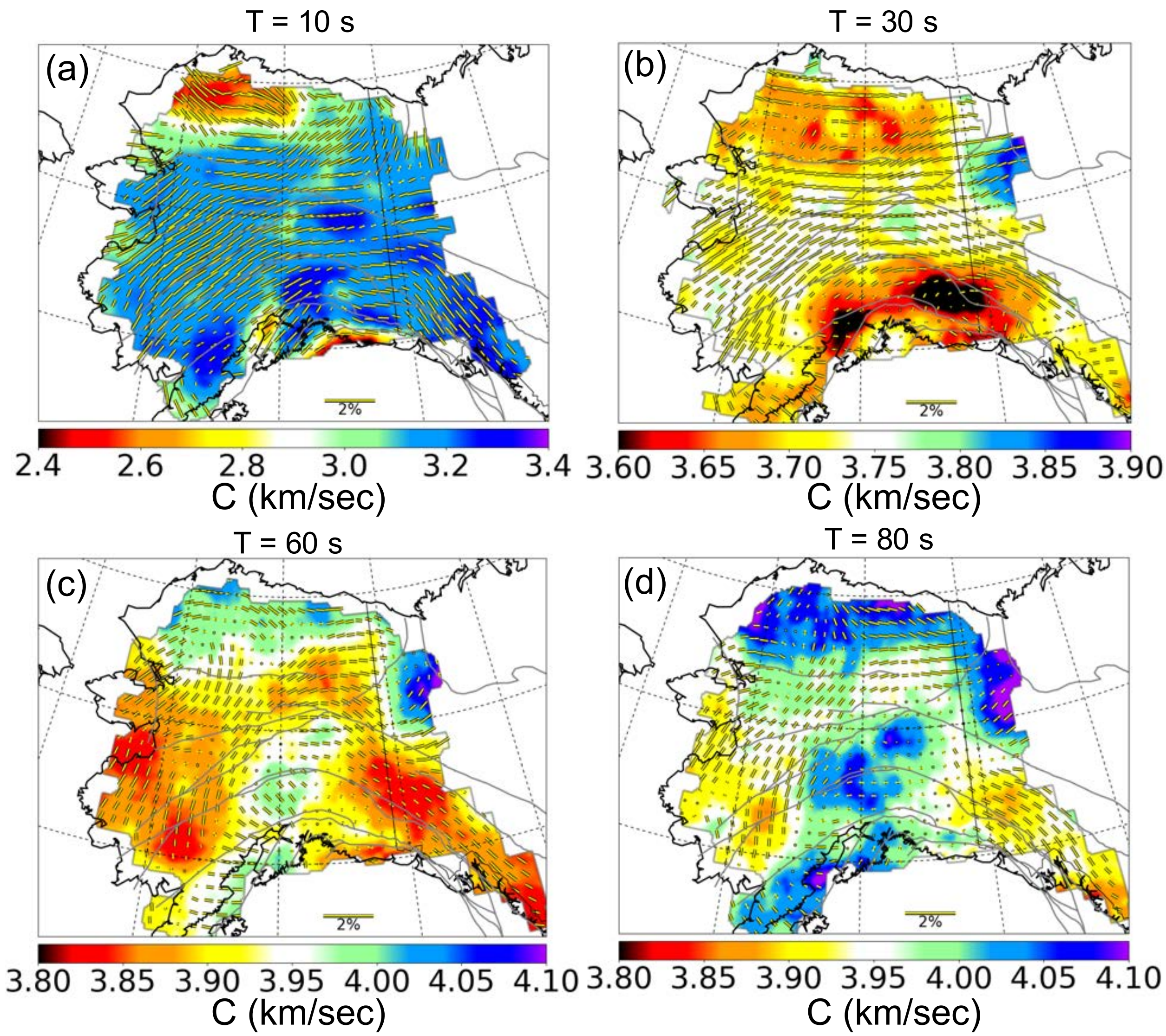

Figure 4. Example Rayleigh wave azimuthal anisotropy maps overplotted on isotropic phase speed for the final data set constructed from a combination of ambient noise and earthquake measurements at periods of: (a) 10 s, (b) 30 s, (c) 60 s, and (d) 80 s.

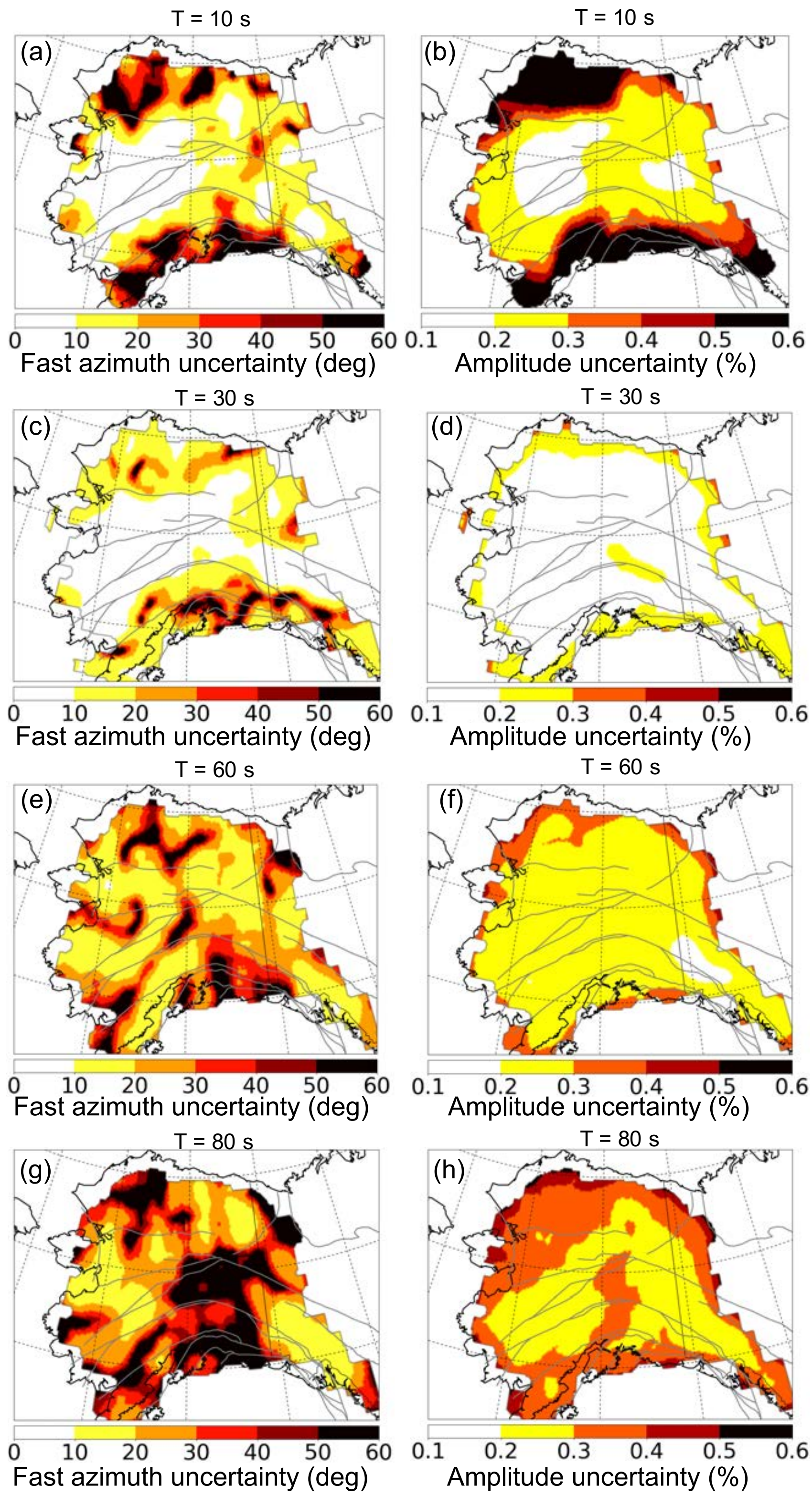

Figure 5. Example maps of one standard deviation uncertainty estimates in fast azimuth and anisotropy amplitude at periods of: (a)-(b) 10 s, (c)-(d) 30 s, (e)-(f) 60 s, and (g)-(h) 80 s.

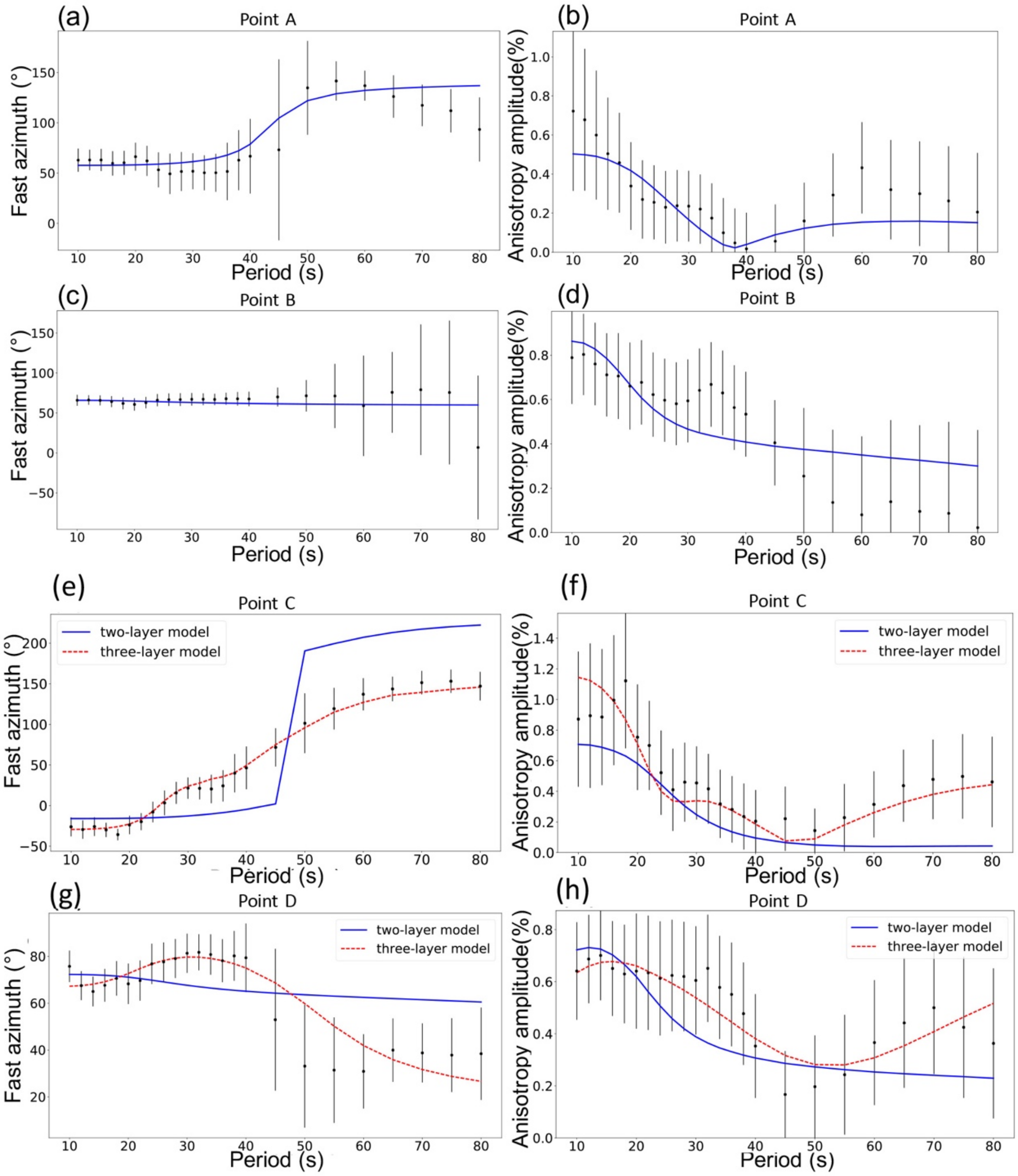

Figure 6. Anisotropy dispersion curves of fast azimuth, $\phi_{FA}(\omega)$, and amplitude, $A(\omega)$, for the sample points A – D identified in **Figure 1**. One standard deviation errors bars are observations from cuves such as those in **Figure 2**, the blue lines are predictions from the Simplified Two-Layer Model of azimuthal anisotropy and red lines are predictions from a Three-Layer Model where a second mantle layer is included. At points A and B the Simplified Two-Layer Model fits the data, but at C and D a second mantle layer must be added to fit the data. (a) - (b) Point A. (c) – (d) Point B. (e) – (f) Point C. (g) – (h) Point D.

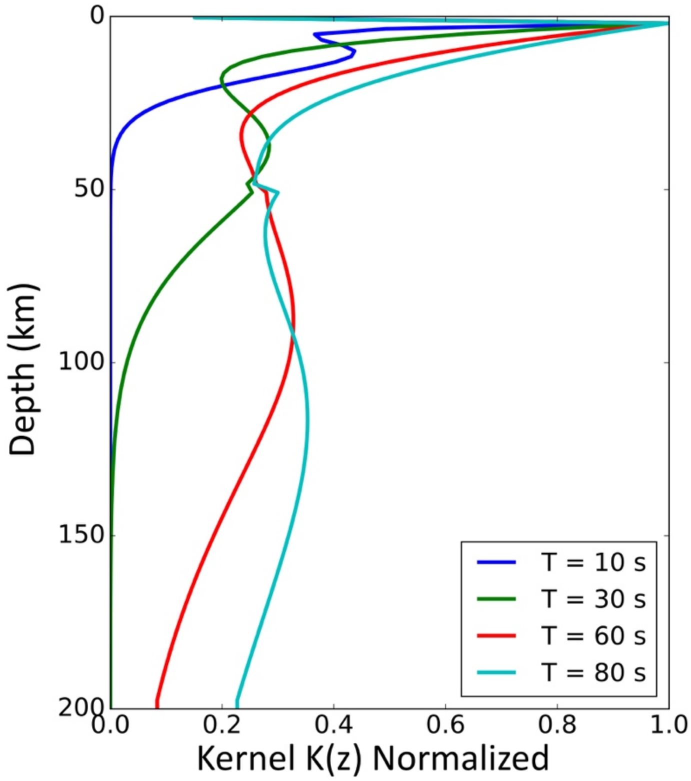

Figure 7. Examples of integral kernels, $\mathbf{K(z)}$, from equation (3) at periods of 10 s, 30 s, 60 s, and 80 s. Kernels are normalized by their maximum amplitude so that each normalized kernel has an amplitude of unity. Peak amplitudes of the non-normalized kernels decrease with period.

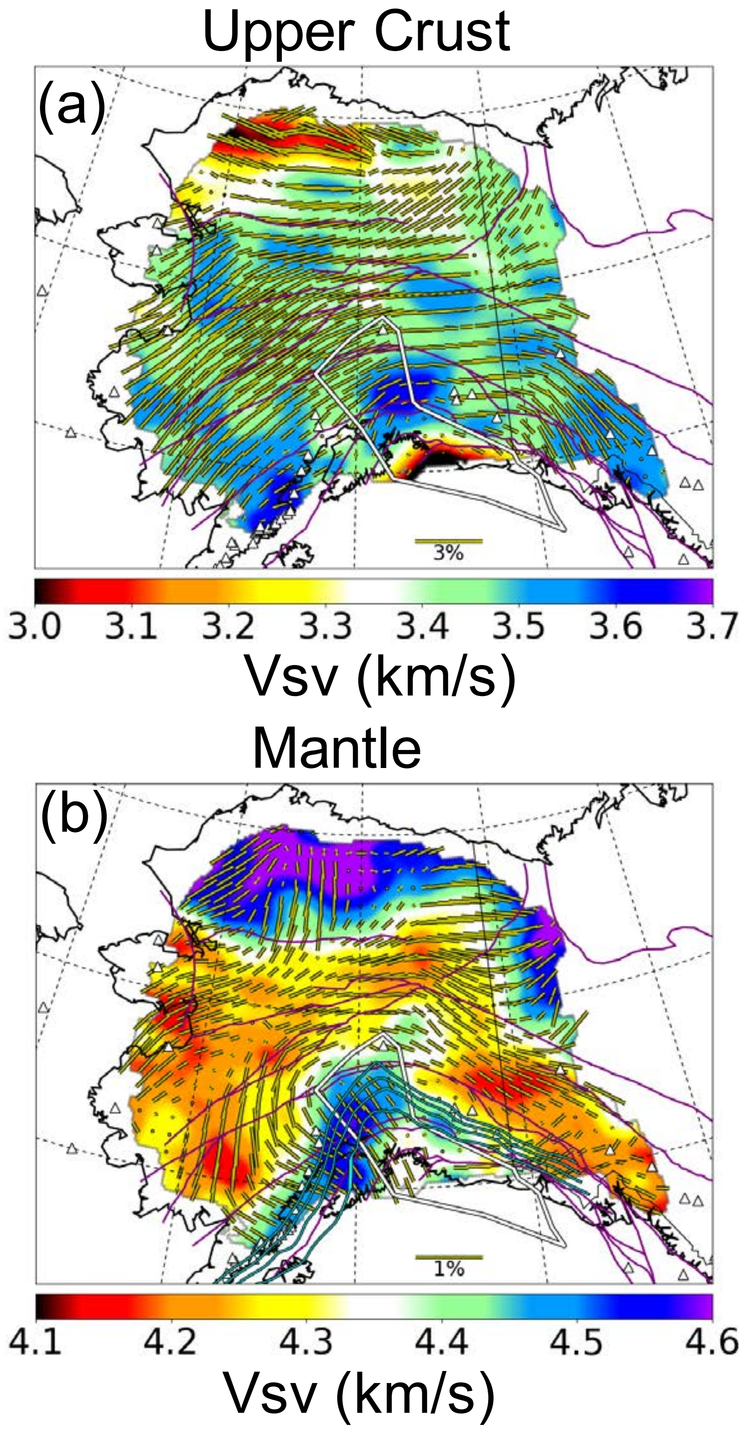

Figure 8. Simplified Two-Layer model of azimuthal anisotropy. (a) Upper crustal azimuthal anisotropy from the base of the sediments to 15 km depth, the background color indicates Vsv at 10 km depth. (b) Mantle azimuthal anisotropy from Moho to 200 km, the background color indicates Vsv at 100 km depth. Faults, the hypothesized Yakutat terrane, volcanoes, and the top slab edges from 40 to 100 km are as in **Figure 1**.

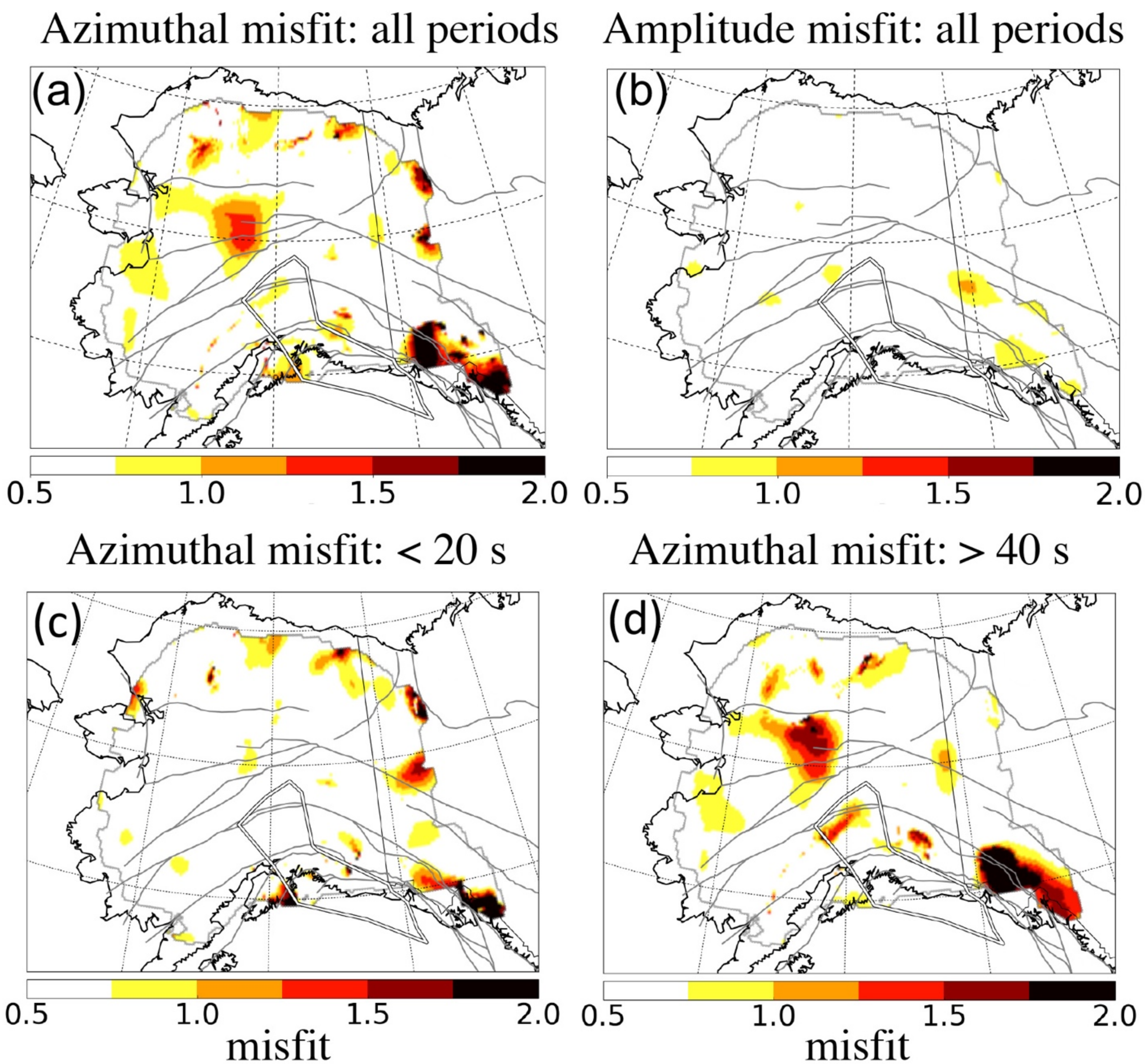

Figure 9. Misfit values (eqn. (6)) computed for the Simplified Two-Layer model for fast azimuth and anisotropy amplitude. (a) Azimuthal misfit taken over all periods. (b) Amplitude misfit taken over all periods. (c) Azimuthal misfit taken only over periods less than or equal to 20 s. (d) Azimuthal misfit taken only over periods greater than or equal to 40 s.

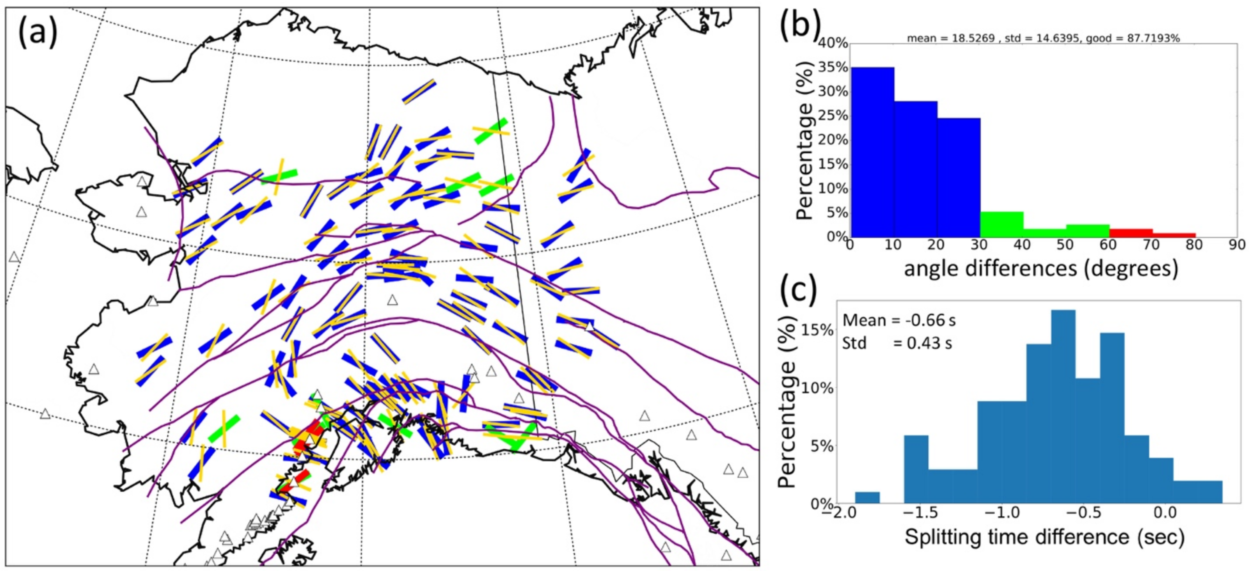

Figure 10. (a) Comparison of fast directions in the mantle part of our model (Simplified Two-Layer model) and those from SKS splitting (Venereau et al., 2019). The yellow bars are mantle fast directions from our model while other colors are the fast axes from SKS splitting: (blue bars) differences in fast directions are less than 30°, (green bars) differences are from 30° - 60°, and (red bars) differences greater than 60°. (b) Histogram of angle differences between our mantle model and SKS; about 88% of locations have an angle difference smaller than 30°. (c) Histogram of differences between predicted SKS splitting time from our mantle model and the observed SKS splitting time, subtracting each observed value from the associated predicted value. The mean and standard deviation of the differences are indicated.